

Iso-geometric Collocation Method for the Fractional Laplacian in the 2D Bounded Domain[☆]

Kailai Xu^a, Eric Darve^b

^a*Institute for Computational and Mathematical Engineering, Stanford University, Stanford, CA, 94305*

^b*Mechanical Engineering, Stanford University, Stanford, CA, 94305*

Abstract

We consider the iso-geometric analysis for fractional PDEs involving the fractional Laplacian in two-dimension. An iso-geometric collocation method is developed to discretize the fractional Laplacian and applied to the fractional Poisson problem and the time-dependent fractional porous media equation. Numerical studies exhibit monotonous convergence with a rate $\mathcal{O}(N^{-1})$, where N is the degrees of freedom. Comparison with finite element analysis shows that the method enjoys higher accuracy per degree of freedom and better convergence rate. We demonstrate that iso-geometric analysis is a promising tool and opens a new venue for nonlocal problems.

Keywords: Iso-geometric Analysis, Fractional Laplacian, Singularity Subtraction

1. Introduction

We consider the nonlocal model in two-dimension involving the Riesz fractional Laplacian, which can be defined through the Fourier transform [1]

$$\mathcal{F}((-\Delta)^s u)(\boldsymbol{\xi}) = |\boldsymbol{\xi}|^{2s} \mathcal{F}(u)(\boldsymbol{\xi}) \quad (1)$$

where $s \in (0, 1)$ and \mathcal{F} is the Fourier transform; or equivalently when u is sufficiently smooth

$$(-\Delta)^s u(\mathbf{x}) = c_{s,2} \text{p.v.} \int_{\mathbb{R}^2} \frac{u(\mathbf{x}) - u(\mathbf{y})}{|\mathbf{x} - \mathbf{y}|^{2+2s}} d\mathbf{y} \quad (2)$$

where p.v. denotes principal integration and $c_{s,2}$ is the normalization constant

$$c_{s,2} = \frac{2^{2s} \Gamma(1+s)}{\pi |\Gamma(-s)|} \quad (3)$$

[☆]The first author thanks the Stanford Graduate Fellowship in Science & Engineering and the 2018 Schlumberger Innovation Fellowship for the financial support.

Email addresses: kailaix@stanford.edu (Kailai Xu), darve@stanford.edu (Eric Darve)

Many applications can be modeled by partial differential equations involving the fractional Laplacian such as the reverse time migration (RTM) for attenuating media [2], the anomalous diffusion in porous media [3], image denoising [4], and so on. For a more comprehensive treatment involving the theory and numerical methods of fractional Laplacian, we refer to the review paper [5].

However, solving the fractional partial differential equations is challenging. One of the challenges is that the kernel Eq. (2) is singular and therefore requires similar techniques for treating singular integrals in the boundary element method. The implementation can be quite challenging, especially in the high dimensional case. Acosta et al. [6] apply the Duffy-type transforms and builds different quadrature rules according to the relative position of two triangle elements (i.e., identical, sharing a vertex, sharing an edge and disjoint). Another challenge is that with homogeneous boundary conditions, the solutions to the fractional Poisson equation are usually only continuous but do not have continuous derivatives. This compromises the convergence rate of many numerical methods. Other challenges include the memory and computation requirement since the resulted linear system is usually dense. Therefore, designing an easy-to-implement and accurate numerical method is desirable.

Many existing methods suffer from their applicability or numerical issues. For example, [7] proposes a radial basis function collocation method for decoupled fractional Laplacian wave equations. The resulting linear system is usually ill-conditioned due to its meshless nature. [8] proposed a “walk-on-spheres” Monte Carlo methods for the fractional Laplacian. The method requires large number of simulation, especially for small s , where the “jump size” is very large thus the variance is large. [9] proposed a spectral method for 2D and 3D but the method is only limited to the unit ball domains.

Since the seminal paper by Hughes et al. [10], there has been extensive research on the iso-geometric analysis. The basic idea of the NURBS-based iso-geometric analysis is to pass from the geometry initially provided by a CAD system to a form suitable for computational analysis. The foundation of the recent work on iso-geometric analysis is based on NURBS to define both the geometry and the solution space [11]. One advantage of iso-geometric analysis is that the defined geometry can be systematically enriched without altering the geometry or its parametrization [12].

This inspired us to initiate a systematic study of nonlocal models involving the fractional Laplacian with the iso-geometric collocation method. We show that compared to the finite element analysis [6, 13], the iso-geometric collocation method is much easier to implement and is more accurate per degree of freedom due to its smooth basis functions. It can also represent the boundaries of various geometry exactly such as a disk, which is difficult for finite difference methods [14, 15]. The application of iso-geometric analysis opens a new venue for solving the fractional differential equations or in general the nonlocal models.

The article is organized as follows. In Section 2, we introduce the iso-geometric collocation methods. In Section 3, we describe the algorithms used for solving the fractional Poisson problem, where we construct the interpolation matrix and the discrete fractional Laplacian matrix, which are used to solve the time-dependent porous media equation in Section 4. In Section 4 we perform the numerical benchmarking on generalized eigenvalues and eigenfunctions of the fractional Laplacian operator. Since we have analytical solutions,

we are able to compare the numerical solution with them and investigate convergence. Besides, we compare the accuracy of the proposed method with the finite element method on a per-degree-of-freedom basis. We also consider an application in the fractional porous media equation. The numerical results show the potential of iso-geometric analysis for nonlocal models and will be the baseline for future work. We conclude in Section 5 and point out future research directions.

For reference, we list all notation used in this paper in Table 1. To facilitate reproducible research, all the codes for this work will be available at <https://github.com/kailaix/ISO2D.jl>.

Notation	Description
s	the fractional index
$c_{s,2}$	the normalization constant in the fractional Laplacian
$(-\Delta)^s$	the fractional Laplacian
$B_{i,p}$	the B-spline basis function
$N_{i,j}$	the NURBS basis function
\mathcal{C}^k	the function space with up to k -th order continuous derivatives
w_i	weights associated with the NURBS basis functions
$\tilde{X}_i, \tilde{\mathbf{X}}_{ij}$	control points
F, \mathbf{F}	mapping from the parameter space to the physical space
\mathbf{V}	the interpolation function space defined by the NURBS basis functions
$\hat{\mathbf{u}}_{ij}, \hat{\mathbf{x}}_{ij}$	the collocation points in the parameter and physical space
ρ, a	the window function and the window size
$(-\Delta)_h$ ($(-\Delta)_h^s$)	the discrete (fractional) Laplacian
\mathbf{M}	the interpolation matrix
\mathbf{L}	the discrete fractional Laplacian matrix

Table 1: Notation used in this paper

2. Iso-geometric Collocation Method

In iso-geometric analysis, the basis functions for approximating the solutions are non-uniform rational basis splines (NURBS). These basis functions emanate from computer aided geometric design (CAGD) instead of the Lagrange finite element interpolation polynomials used in finite element analysis [16]. In this section, we present an overview of the iso-geometric collocation method. For details on iso-geometric analysis, see the appendix.

Consider the generalized boundary-value problem

$$\mathcal{L}u = f \text{ in } \Omega, \quad u = 0 \text{ in } \Omega^c \quad (4)$$

where the solution $u : \mathbb{R}^2 \rightarrow \mathbb{R}$ has compact support in Ω and \mathcal{L} is a nonlocal operator, e.g., the fractional Laplacian $(-\Delta)^s$. f is the given data.

We introduce a NURBS representation of Ω . The collocation points is a finite set in the parameter space $\{\hat{\mathbf{u}}_i\}_{i \in \mathcal{I}}$, where $\mathcal{I} = \mathcal{I}_D \cup \mathcal{I}_L$ is divided into two distinct sets [12]. The

points in \mathcal{I}_D lie on $\partial\Omega$ while those in \mathcal{I}_L are inside Ω . Then, the iso-geometric collocation methods find $u_h \in \mathbf{V}$ such that

$$\mathcal{L}u_h(\mathbf{F}(\hat{\mathbf{u}}_i)) = f(\mathbf{F}(\hat{\mathbf{u}}_i)) \quad i \in \mathcal{I}_L \quad (5)$$

$$u_h(\mathbf{F}(\hat{\mathbf{u}}_i)) = 0 \quad i \in \mathcal{I}_D \quad (6)$$

A common used set of collocation points is derived from the Greville abscissae [17]. The Greville abscissae \bar{u}_i is related to the knot vector $\{u_1, u_2, \dots, u_{l+1}\}$ through

$$\bar{u}_i = \frac{u_{i+1} + u_{i+2} + \dots + u_{i+p}}{p} \quad (7)$$

Analogously, in two dimension, we can construct the Greville abscissae \bar{u}_i, \bar{v}_j for both dimensions and consider the tensor product

$$\hat{\mathbf{u}}_{ij} = (\bar{u}_i, \bar{v}_j) \quad \hat{\mathbf{x}}_{ij} = \mathbf{F}(\hat{\mathbf{u}}_{ij}) \quad (8)$$

Then the iso-geometric analysis collocation method with Greville abscissae reads: find $u_h \in \mathbf{V}$ such that

$$\mathcal{L}u_h(\hat{\mathbf{x}}_{ij}) = f(\hat{\mathbf{x}}_{ij}) \quad i = 2, 3, \dots, l_u - p - 1; j = 2, 3, \dots, l_v - q - 1 \quad (9)$$

$$u_h(\hat{\mathbf{x}}_{ij}) = 0 \quad (i, j) \in \{1, l_u - p\} \times \{1, 2, \dots, l_v - q\} \cup \{1, 2, \dots, l_u - p\} \times \{1, l_v - q\} \quad (10)$$

3. Numerical Scheme

3.1. Singularity Subtraction

In this section we will consider the discretization of the fractional Laplacian operator. Assume the knot vectors for u and v are

$$\{u_1, u_2, \dots, u_{l_u+1}\} \quad \{v_1, v_2, \dots, v_{l_v+1}\} \quad (11)$$

and the degrees are p and q respectively. We assume that the inequalities in Eq. (A.2) hold strictly so that the $\mathbf{V} \subset \mathcal{C}^{\min\{p,q\}-1}$. Let $\hat{\mathbf{u}}_{ij}$ be the collocation points derived from the Greville abscissae, and $\hat{\mathbf{x}}_{ij} = \mathbf{F}(\hat{\mathbf{u}}_{ij})$.

Assume that $u(\mathbf{x}) \in \mathcal{C}^4$, we compute the principal value integral

$$\text{p.v.} \int_{\mathbb{R}^2} \frac{u(\mathbf{x}) - u(\mathbf{y})}{|\mathbf{x} - \mathbf{y}|^{2+2s}} d\mathbf{y}$$

using the singularity subtraction method [15]

$$\int_{\mathbb{R}^2} \frac{u(\mathbf{x}) - u(\mathbf{y})}{|\mathbf{x} - \mathbf{y}|^{2+2s}} d\mathbf{y} = \int_{\mathbb{R}^2} \frac{u(\mathbf{x}) - u(\mathbf{y}) + \rho(|\mathbf{x} - \mathbf{y}|)g_{\mathbf{x}}(\mathbf{y})}{|\mathbf{x} - \mathbf{y}|^{2+2s}} d\mathbf{y} - \int_{\mathbb{R}^2} \frac{\rho(|\mathbf{x} - \mathbf{y}|)g_{\mathbf{x}}(\mathbf{y})}{|\mathbf{x} - \mathbf{y}|^{2+2s}} d\mathbf{y} \quad (12)$$

where ρ is a window function defined by

$$\rho(r) = \begin{cases} 1 - 35 \left(\frac{r}{a}\right)^4 + 84 \left(\frac{r}{a}\right)^5 - 70 \left(\frac{r}{a}\right)^6 + 20 \left(\frac{r}{a}\right)^7 & r < a \\ 0 & \text{otherwise} \end{cases} \quad (13)$$

Here $a > 0$ is the window size and $g_{\mathbf{x}}(\mathbf{y})$ is the truncated Taylor expansion of $u(\mathbf{y}) - u(\mathbf{x})$

$$\begin{aligned} g_{\mathbf{x}}(\mathbf{y}) &:= u_1(\mathbf{x})v_1 + u_2(\mathbf{x})v_2 \\ &+ u_{11}(\mathbf{x})\frac{v_1^2}{2} + u_{22}(\mathbf{x})\frac{v_2^2}{2} + u_{12}(\mathbf{x})v_1v_2 \\ &+ u_{111}(\mathbf{x})\frac{v_1^3}{6} + u_{112}(\mathbf{x})\frac{v_1^2v_2}{2} + u_{122}(\mathbf{x})\frac{v_1v_2^2}{2} + u_{222}(\mathbf{x})\frac{v_2^3}{6} \end{aligned} \quad (14)$$

Here we have used the abbreviation for the derivatives of $\mathbf{v} = (v_1, v_2) = \mathbf{y} - \mathbf{x}$,

$$u_i := \frac{\partial u}{\partial \mathbf{x}_i}, \quad u_{ij} := \frac{\partial^2 u}{\partial \mathbf{x}_{ij}^2}, \quad u_{ijk} := \frac{\partial^3 u}{\partial \mathbf{x}_{ijk}^3}, \quad i, j, k \in \{1, 2\} \quad (15)$$

The function ρ was chosen such that $\rho(r) = 1 + \mathcal{O}(r^4)$, $r \rightarrow 0+$, $u(\mathbf{x}) - u(\mathbf{y}) + \rho(|\mathbf{x} - \mathbf{y}|)g_{\mathbf{x}}(\mathbf{y}) \sim \mathcal{O}(|\mathbf{x} - \mathbf{y}|^4)$, $\mathbf{y} \rightarrow \mathbf{x}$, so that the integrand in

$$\int_{\mathbb{R}^2} \frac{u(\mathbf{x}) - u(\mathbf{y}) + \rho(|\mathbf{x} - \mathbf{y}|)g_{\mathbf{x}}(\mathbf{y})}{|\mathbf{x} - \mathbf{y}|^{2+2s}} d\mathbf{y} \quad (16)$$

is continuous, thus integrable. Figure 1 shows $\frac{u(\mathbf{x}) - u(\mathbf{y}) + \rho(|\mathbf{x} - \mathbf{y}|)g_{\mathbf{x}}(\mathbf{y})}{|\mathbf{x} - \mathbf{y}|^{2+2s}}$ and $\frac{|u(\mathbf{x}) - u(\mathbf{y})|}{|\mathbf{x} - \mathbf{y}|^{2+2s}}$ for $s = 0.3$. We can see that by singularity subtraction, the integrand is turned into a continuous function suitable for standard numerical quadrature rule. The window function is shown in Figure 2.

Due to symmetry, we have for the second part in Eq. (12)

$$\int_{\mathbb{R}^2} \frac{\rho(|\mathbf{x} - \mathbf{y}|)g_{\mathbf{x}}(\mathbf{y})}{|\mathbf{x} - \mathbf{y}|^{2+2s}} d\mathbf{y} = \frac{1}{2} \Delta u(\mathbf{x}) \int_{\mathbb{R}^2} \frac{\rho(|\mathbf{y}|)y_1^2}{|\mathbf{y}|^{2+2s}} d\mathbf{y} \quad (17)$$

3.2. Numerical Discretization

We now adopt the standard numerical quadrature for computing Eq. (16). The idea is that for a function in 2D we can express it in the polar coordinates

$$\int_{\mathbb{R}^2} f(\mathbf{x}) d\mathbf{x} = \int_0^\infty dr \int_{\mathbb{S}^1} r f(r\boldsymbol{\sigma}) d\boldsymbol{\sigma} \quad (18)$$

where \mathbb{S}^1 is the unit circle. The numerical quadrature is constructed from the tensor product of the Gauss Legendre quadrature rule in the radial direction and trapezoidal rule in the axial direction, i.e.,

$$\boldsymbol{\xi}_{ij} = r_i \boldsymbol{\sigma}_j, \quad w_{ij}^Q = \frac{2\pi w_i^{GL} r_i}{m}, \quad i = 1, 2, \dots, n; \quad j = 1, 2, \dots, m \quad (19)$$

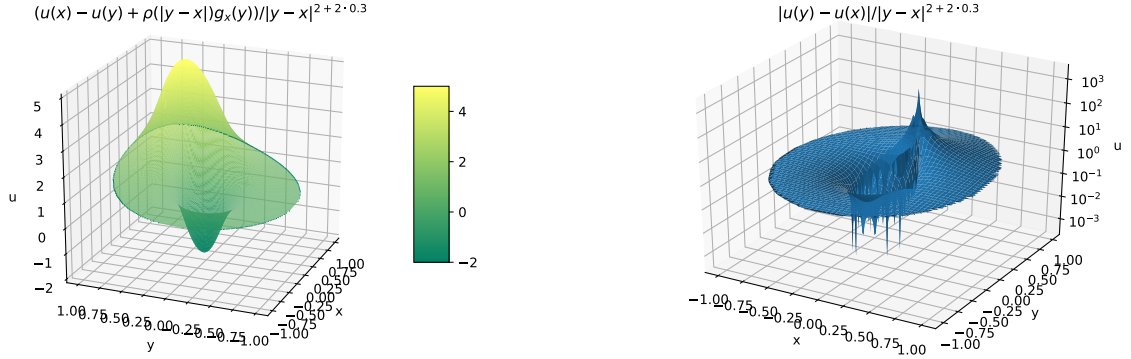


Figure 1: $\frac{u(\mathbf{x}) - u(\mathbf{y}) + \rho(|\mathbf{x} - \mathbf{y}|)g_{\mathbf{x}}(\mathbf{y})}{|\mathbf{x} - \mathbf{y}|^{2+2s}}$ and $\frac{|u(\mathbf{x}) - u(\mathbf{y})|}{|\mathbf{x} - \mathbf{y}|^{2+2s}}$ for $s = 0.3$ and $u(\mathbf{x}) = (1 - |\mathbf{x}|^2)^{1+s}$. The function on the left is continuous while the one on the right has a singularity. By singularity subtraction, the integrand is turned into a continuous function suitable for a standard numerical quadrature rule. Note that the derivative of the integrand is not necessarily continuous.

where (r_i, w_i^{GL}) are Gauss Legendre quadrature points and weights in $[0, R]$ for a sufficient large R . Therefore, Eq. (16) can then be discretized as

$$\sum_{i=1}^n \sum_{j=1}^m \frac{2\pi w_{ij}^{GL}}{m} \frac{u(\mathbf{x}) - u(\mathbf{x} + \boldsymbol{\xi}_{ij}) + \frac{\rho_i r_i^2 \Delta u(\mathbf{x})}{2}}{r_i^{1+2s}} \quad (20)$$

here $\rho_i = \rho(r_i)$. For the Laplacian operator Δ , we consider the fourth order discretization [18]

$$\Delta u(\mathbf{x}) \approx \Delta_h u(\mathbf{x}) = \sum_{i=1}^2 \frac{-\frac{1}{12}u(\mathbf{x} - 2\mathbf{e}_i h) + \frac{4}{3}u(\mathbf{x} - \mathbf{e}_i h) - \frac{5}{2}u(\mathbf{x}) + \frac{4}{3}u(\mathbf{x} + \mathbf{e}_i h) - \frac{1}{12}u(\mathbf{x} + 2\mathbf{e}_i h)}{h^2} \quad (21)$$

here $\mathbf{e}_1 = \begin{bmatrix} 1 \\ 0 \end{bmatrix}$, $\mathbf{e}_2 = \begin{bmatrix} 0 \\ 1 \end{bmatrix}$. Note we require $u(\mathbf{x}) \in \mathcal{C}^4$ to obtain the fourth order estimate of the discretization Eq. (21).

Define

$$A = 2\pi \sum_{i=1}^n \frac{w_{ij}^{GL}}{r_i^{1+2s}}, \quad B = \sum_{i=1}^n \frac{\pi w_{ij}^{GL} \rho_i}{r_i^{2s-1}} - \pi \int_0^a \frac{\rho(r)}{r^{2s-1}} dr$$

then the discretization of the fractional Laplacian operator is given as

$$(-\Delta)^s u(\mathbf{x}) \approx (-\Delta)_h^s u(\mathbf{x}) = c_{s,2} \left(Au(\mathbf{x}) - \sum_{i=1}^n \sum_{j=1}^m \frac{2\pi w_{ij}^{GL}}{mr_i^{1+2s}} u(\mathbf{x} + \boldsymbol{\xi}_{ij}) + B\Delta_h u(\mathbf{x}) \right) \quad (22)$$

We pick a sufficient large R so that the computational domain Ω is contained in the convex hull of the numerical quadrature points. Only the terms where $\mathbf{x} + \boldsymbol{\xi}_{ij} \in \Omega$ do not vanish in the second summation Eq. (22). Figure 3 depicts such an example where Ω is the unit disk and $\mathbf{x} + \boldsymbol{\xi}_{ij}$ corresponding to the non-vanishing terms for two \mathbf{x} 's are shown.

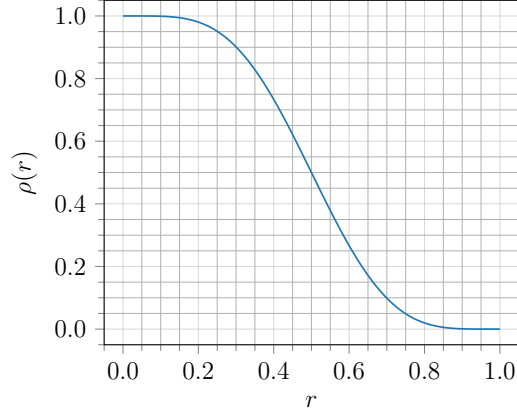


Figure 2: An example of the window function Eq. (13) for $a = 1$. The function behaves like $1 - \mathcal{O}(r^4)$ near the origin.

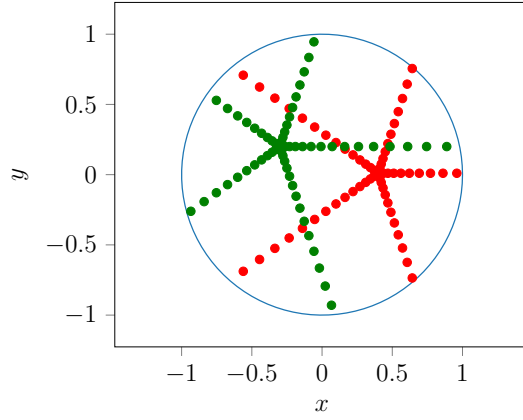


Figure 3: An example of quadrature points used in evaluating the second term in Eq. (22).

3.3. Interpolation Matrix and the Discrete Fractional Laplacian Matrix

Let us consider any point $\mathbf{x} \in \Omega$, then there exists $\mathbf{u} = \begin{bmatrix} u \\ v \end{bmatrix}$ in the parameter space such that $\mathbf{F}(\mathbf{u}) = \mathbf{x}$. The numerical solution $u_h \in \mathbf{V}$ can be written as

$$u_h(\mathbf{x}) = u_h(\mathbf{F}^{-1}(\mathbf{u})) := \sum_{i=1}^{l_u-p} \sum_{j=1}^{l_v-q} N_{i,j}(u, v) c_{ij} \quad (23)$$

Since every NURBS basis function only spans pq patches in the parameter space, thus no more than pq terms in the summation in Eq. (23) are nonzero. If we consider the collocation points derived from Greville abscissae, we have

$$u_h(\hat{\mathbf{x}}) = \mathbf{M}\mathbf{c} \quad (24)$$

where $\hat{\mathbf{x}} = \text{vec}(\{\hat{\mathbf{x}}_{ij}\}_{i=1,2,\dots,l_u-p; j=1,2,\dots,l_v-q})$, $\mathbf{c} = \text{vec}(\{c_{ij}\})$ and \mathbf{M} is a sparse matrix with at most pq non-zeros per row. Here vec is the vectorization of a matrix,

$$\text{vec}(\{\mathbf{x}_{ij}\}_{ij}) = [\mathbf{x}_{11}, \dots, \mathbf{x}_{l_u-p,1}, \mathbf{x}_{12}, \dots, \mathbf{x}_{l_u-p,2}, \dots, \mathbf{x}_{1,l_v-q}, \dots, \mathbf{x}_{l_u-p,l_v-q}]^T \quad (25)$$

We call \mathbf{M} the *interpolation matrix*, which maps the coefficients from the parameter space to point-wise values in the physical space and vice versa.

To materialize Eq. (22), assume that $u(\mathbf{x})$ is given in terms of the coefficients \mathbf{c} in the parameter space, then we can evaluate the values of u at the evaluating points \mathbf{x} , $\mathbf{x} + \boldsymbol{\xi}_{ij}$, $\mathbf{x} \pm h\mathbf{e}_i$, $\mathbf{x} \pm 2h\mathbf{e}_i$ using Eq. (23). The values are computed and plugged into Eq. (22) to obtain the values $(-\Delta)_h^s u(\mathbf{x})$. The process is a composition of linear operators and maps the coefficients in the parameter space to the point-wise values of the fractional Laplacian in the physical space. If the collocation points are $\{\hat{\mathbf{x}}_{ij}\}$, we denote the associated linear operator, a.k.a, a matrix, as \mathbf{L} , i.e.,

$$(-\Delta)_h^s u(\hat{\mathbf{x}}) = \mathbf{L}\mathbf{c} \quad (26)$$

The interpolation matrix \mathbf{M} and the discrete fractional Laplacian matrix \mathbf{L} can be pre-computed. Algorithm 1 shows the algorithm for solving the Poisson equation using the matrices mentioned above.

Algorithm 1 Solving the fractional Poisson problem using the interpolation matrix and the discrete fractional Laplacian matrix.

- 1: **Input:** f **Output:** $u_h(\hat{\mathbf{x}}_{ij})$
 - 2: Precompute \mathbf{L} , \mathbf{M}
 - 3: $\mathbf{f} \leftarrow \text{vec}(\{\mathbf{f}_{ij}\}_{ij})$ where $\mathbf{f}_{ij} = f(\hat{\mathbf{x}}_{ij})$
 - 4: $\mathbf{f}[\mathcal{I}_D] \leftarrow 0$ {Recall that \mathcal{I}_D are the DOFs associated with boundaries.}
 - 5: $\mathbf{L}[\mathcal{I}_D, :] = \mathbf{M}[\mathcal{I}_D, :]$ {Impose the zero boundary conditions.}
 - 6: $\mathbf{c} \leftarrow \mathbf{L}^{-1}\mathbf{f}$
 - 7: **return** $\mathbf{M}\mathbf{c}$
-

3.4. Convergence and Error Bounds

The choice m and n in the numerical quadrature rule Eq. (19) as well the choice of step size h in Eq. (21) affects the accuracy of the numerical scheme. As we show in the numerical examples, these parameters will influence the accuracy lower bound while have little impact on the convergence rate.

The approximation ability depends on the number of knots, the degrees as well as the mesh structure of the NURBS surface. It is shown that under appropriate assumptions, the NURBS space on the physical domain delivers the optimal rate of the convergence, similar to the finite element space of degree p [19]. The following lemma gives the global error estimate

Lemma 1. *Let k and l be integer indices with $0 \leq k \leq l \leq p + 1$, we have*

$$\sum_{K \in \mathcal{K}_h} \|v - \Pi_{\mathcal{V}_h} v\|_{\mathcal{H}_h^k(K)}^2 \leq C_{\text{shape}} \sum_{K \in \mathcal{K}_h} h_K^{2(l-k)} \sum_{i=0}^l \|\nabla F\|_{L^\infty(F^{-1}(K))}^{2(i-l)} |v|_{H^i(K)}^2 \quad \forall v \in H^l(\Omega) \quad (27)$$

December 15, 2024

For the proof the readers are referred to [19]. Here \mathcal{K}_h are the patches in the parametric space, \mathcal{V}_h is the NURBS space, C_{shape} is a constant depending on the structure of the NURBS surface, H^i is the standard Sobolev space, h_K is the diameter of K , and $\mathcal{H}_h^k(K)$ are patches in the physical space endowed with its own norms. The lemma indicates that if v is sufficiently smooth, increasing the degree of the NURBS surface (p -refinement) or the number of control points (h -refinement) will yield better approximations. However, it may not be the case for less smooth functions, where are often encountered in the PDEs involving the fractional Laplacian [20].

We assume that the domain Ω satisfies the exterior ball condition, i.e., there exists a positive radius ρ_0 such that all the points on $\partial\Omega$ can be touched by some exterior ball of radius ρ_0 . The solution to the fractional Poisson equation (Eq. (4)) with $\mathcal{L} = (-\Delta)^s$ is only Hölder continuous according to Corollary 1.6 in [20].

Lemma 2. *Let Ω be a bounded $C^{1,1}$ domain satisfying the exterior ball condition, $f \in L^\infty(\Omega)$, u be a solution of Eq. (4) with $\mathcal{L} = (-\Delta)^s$. Then,*

$$u \in C^{0,s}(\mathbb{R}^2) \quad \text{and} \quad \|u\|_{C^{0,s}} \leq C \|f\|_{L^\infty(\Omega)}$$

where C is a constant depending only on Ω and s .

The lemma indicates that the solution is Hölder continuous. In fact, it is also shown [20] that $\frac{u}{\delta^s}$ is continuous in $\bar{\Omega}$, i.e., the solution is continuous but not continuously differentiable near the boundary. For the case $s > \frac{1}{2}$, we have the following estimate

Theorem 1. *Assume that Ω is a bounded $C^{1,1}$ domain satisfying the exterior ball condition, $f \in L^\infty(\Omega)$, u be a solution of Eq. (4) with $\mathcal{L} = (-\Delta)^s$, $s > \frac{1}{2}$. In addition, assume that the mesh is quasi-uniform, i.e., there exists $\gamma_1 \leq 1 \leq \gamma_2$, such that*

$$\gamma_1 h \leq h_K \leq \gamma_2 h \quad \forall K \in \mathcal{K}_h \quad (28)$$

then there exists $C > 0$ such that

$$\sum_{K \in \mathcal{K}_h} \|u - \Pi_{\mathcal{V}_h} u\|_{L^2(\Omega)}^2 \lesssim h^2 \quad (29)$$

To prove Theorem 1, we need the following embedding lemma between Sobolev space and Hölder space [21]

Lemma 3. *Assume that Ω is a bounded $C^{1,1}$ domain, $m, k \in \mathbb{N}_0$, $p \in [1, \infty)$, $\alpha \in [0, 1]$.*

$$m - \frac{n}{p} \leq k + \alpha \quad \alpha \neq 0, 1 \quad (30)$$

then $W^{m,p}(\Omega) \subset C^{k,\alpha}(\bar{\Omega})$ and there is a constant $C > 0$, s.t.

$$\|u\|_{W^{m,p}(\Omega)} \leq C \|u\|_{C^{k,\alpha}(\Omega)} \quad (31)$$

If $m - \frac{n}{p} < k + \alpha$, the embedding is compact.

Proof of Theorem 1. Due to Lemma 2, the solution is s -Hölder continuous. Let $n = p = 2$, $m = 1$, $k = 0$, $\alpha = s$ in Lemma 3, we have

$$\|u\|_{H^1} \leq C \|u\|_{C^{0,s}(\Omega)} \quad (32)$$

for a constant $C > 0$. We invoke Lemma 1 with $l = 1$, $k = 0$, and thus have

$$\sum_{K \in \mathcal{K}_h} \|u - \Pi_{\mathcal{V}_h} u\|_{L^2(\Omega)}^2 \lesssim h^2 \quad (33)$$

□

Note for the case $s \leq \frac{1}{2}$ the proof is not applicable. However, we observe numerically that we still obtain the $\mathcal{O}(h^2)$ convergence rate.

Another source of error is the numerical error of solving the linear system $\mathbf{L}\mathbf{c} = \mathbf{f}$ in Algorithm 1. The condition number of \mathbf{L} grows as we increase the number of control points. The convergence of the iterative solver such as GMRES may be slow if no proper preconditioner is used. In fact, it is shown that for finite element methods, if a family of shape regular and globally quasi-uniform triangulations with maximal element size h is used, the stiffness matrix satisfies [22]

$$\kappa(\mathbf{L}) = Ch^{-2s} \quad (34)$$

In the paper we have used Greville abscissae as the collocation points, which have been widely adopted as the default choice in the iso-geometric analysis literature [23].

4. Numerical Experiments

4.1. Numerical Benchmark

For verification and benchmarking we consider the generalized eigenvalue problem for $(-\Delta)^s$ in a unit disk $\Omega \subset \mathbb{R}^d$, with a zero condition in the complement of Ω

$$\begin{cases} (-\Delta)^s ((1 - |\mathbf{x}|^2)^s \varphi_n(\mathbf{x})) = \lambda_n \varphi_n(\mathbf{x}) & \mathbf{x} \in \Omega \\ \varphi_n(\mathbf{x}) = 0 & \mathbf{x} \notin \Omega \end{cases} \quad (35)$$

where $n = 0, 1, \dots$. The eigenvalues λ_n and the eigenfunctions $\varphi_n(\mathbf{x})$ are given as [24]

$$\lambda_n = \frac{2^{2s} \Gamma(s + n + 1)^2}{(n!)^2} \quad \varphi_n(\mathbf{x}) = (-1)^n P_n^{(s,0)}(2|\mathbf{x}|^2 - 1)$$

We assume the right hand side $\lambda_n \varphi_n(\mathbf{x})$ is given and apply the proposed algorithm Algorithm 1 to obtain the numerical solution $u_h(\hat{\mathbf{x}}_{ij})$. The error is computed using

$$\text{error} = \sqrt{\frac{\sum_{i,j} |u_h(\hat{\mathbf{x}}_{ij}) - (1 - |\hat{\mathbf{x}}_{ij}|^2)^s \varphi_n(\hat{\mathbf{x}}_{ij})|^2}{(l_u - p)(l_v - q)}} \quad (36)$$

here $(1 - |\hat{\mathbf{x}}_k|^2)^s \varphi_n(\hat{\mathbf{x}}_k)$ is the exact solution at $\hat{\mathbf{x}}_k$.

The numerical experiments are carried out with parameters $s = 0.8$, $a = 0.1$, $h = 0.001$, $R = 20$, $p = q = 2$, $n = 1, 2, 3, 4, 5$. In the first case we use $m = 20$, $n = 1000$ while in the second case we use $m = 40$, $n = 5000$ (m and n are the number of quadrature points in the axial and radial directions). Figure 4 shows the convergence results for Eq. (35). The first column shows the reference solution. The second column shows the convergence of the algorithm with respect the degrees of freedom N by varying the number of refinements for different number of quadrature points. We have obtained monotonous convergence and observed $\mathcal{O}(N^{-1})$ convergence for all cases, where N is the degrees of freedom. m, n influence the final error while have little impact on the convergence order. Larger numbers of quadrature points yield better accuracy.

Note that the exact solutions $(1 - |\mathbf{x}|^2)^s \varphi_n(\mathbf{x})$ are continuous but not \mathcal{C}^1 on the boundary $|\mathbf{x}| = 1$. However, we observe no difficulty in applying the proposed algorithm even though we have required \mathcal{C}^3 for the singularity subtraction and \mathcal{C}^4 for the fourth order discretization of the Laplacian operator. This is due to the fact that the collocation points derived from the Greville abscissae are usually denser near the boundary and therefore mitigate accuracy loss partially.

4.2. Comparison with FEM

In this section, we compare the accuracy of the proposed algorithm with finite element analysis on a per-degree-of-freedom basis. We solve the same problem in Eq. (35) with $n = 2$ and $s = 0.5$ using iso-geometric analysis as well as finite element analysis [6]. The corresponding finite element analysis codes are made available by the authors.¹ For the finite element method, the error is measured as the mean squared error on the vertices $\tilde{\mathbf{x}}_k$ of the mesh triangles, i.e.

$$\text{error} = \sqrt{\frac{\sum_k |u_h(\mathbf{x}_k) - (1 - |\mathbf{x}_k|^2)^s \varphi_n(\mathbf{x}_k)|^2}{(l_u - p)(l_v - q)}} \quad (37)$$

In Figure 5, we report the log-scale plots of the errors for FEM and iso-geometric analysis (IGA) with $n = 1000$, $m = 20$ and $n = 5000$, $m = 40$. We can see that iso-geometric analysis exhibits superior accuracy compared with finite element analysis for the fractional Laplacian problem. Besides, iso-geometric analysis yields a better convergence rate without particular preprocessing, although the rate can be improved for finite element analysis by adopting the graded meshes [6]. We also point out the iso-geometric analysis code is much easier to implement, while for finite element analysis we need to carefully treat the quadrature rules for the singular kernel. For example, [6] applies the Duffy-type transforms and builds different quadrature rules according to the relative position of two triangle elements (i.e., identical, sharing a vertex, sharing an edge and disjoint).

¹See <https://github.com/fbersetche/A-short-FE-implementation-for-a-2d-homogeneous-Dirichlet-problem-of-a-Fractional-Laplacian>

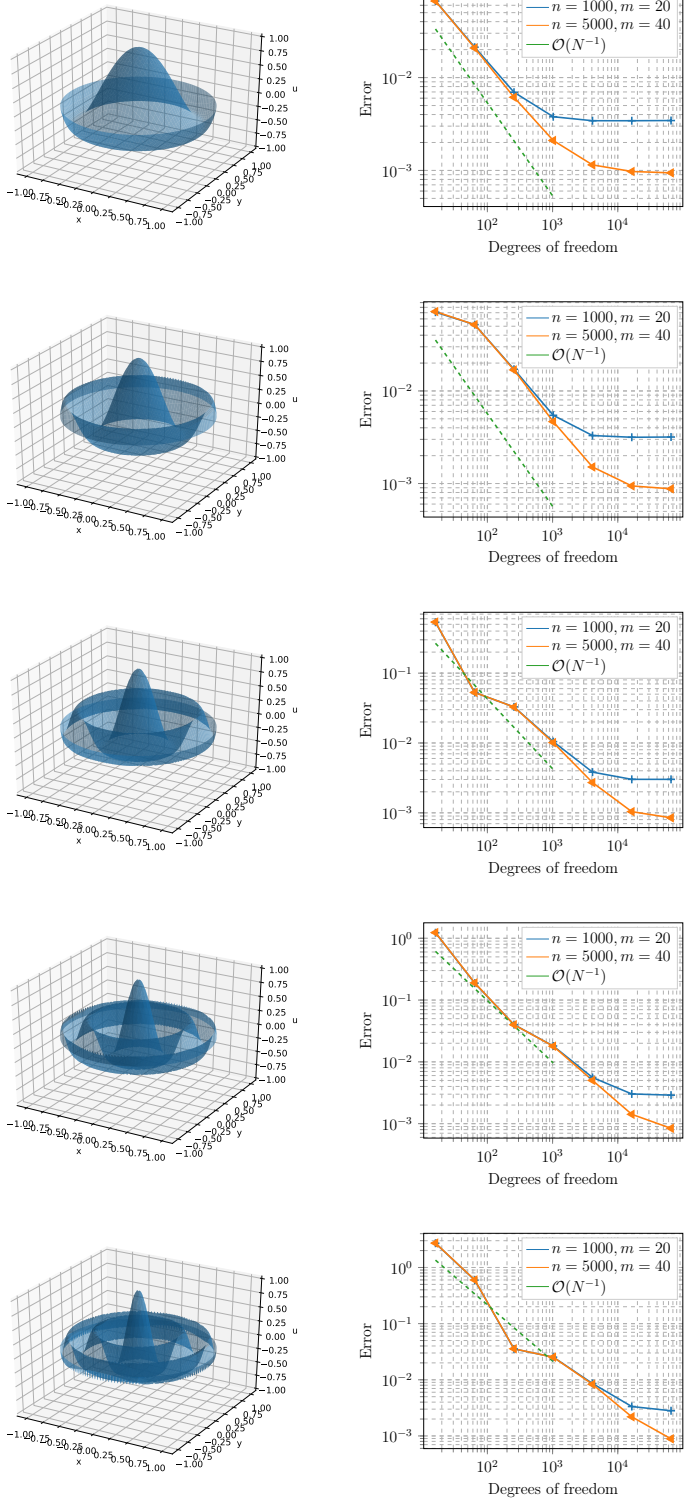


Figure 4: Convergence results for Eq. (35). The first column shows the reference solution. The second column shows the convergence of the algorithm with respect the degrees of freedom N by varying the number of refinements for different number of quadrature points. The parameters m and n are the number of quadrature points in the axial and radial directions.

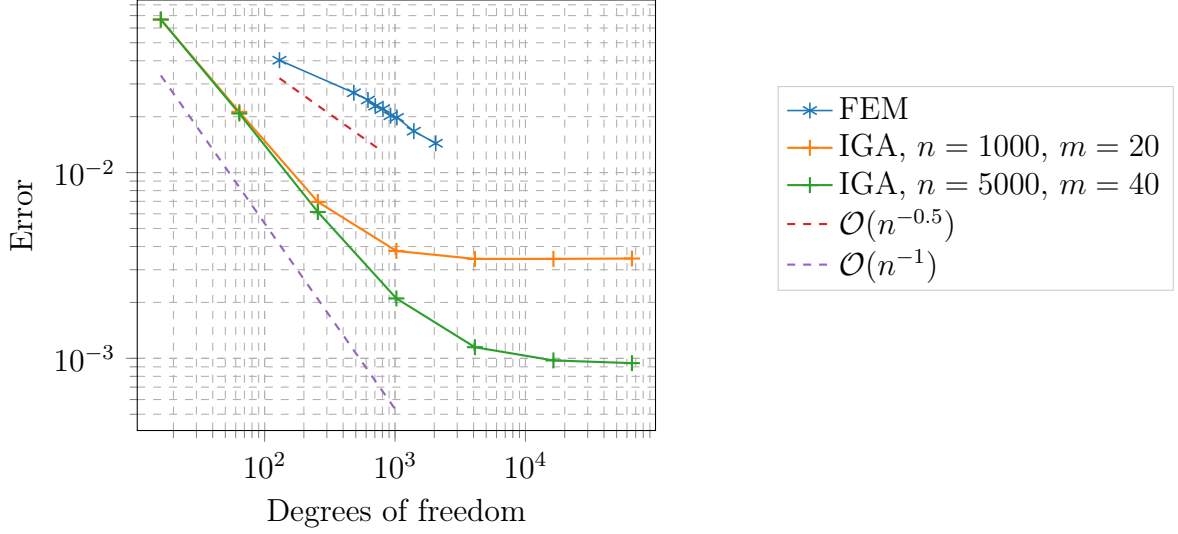


Figure 5: Iso-geometric analysis exhibits superior accuracy compared with finite element analysis for the fractional Laplacian problem.

4.3. Application: Porous Medium Equation with the Fractional Laplacian

This application is concerned with the fractional porous media equation, which describes anomalous diffusion in the porous media [3]

$$\begin{cases} u_t + (-\Delta)^s(|u|^{m-1}u) = 0 & \mathbf{x} \in \mathbb{R}^2, t > 0 \\ u(\mathbf{x}, 0) = f(\mathbf{x}) & \mathbf{x} \in \mathbb{R}^2 \end{cases} \quad (38)$$

We truncate the domain to $[-1, 1]^2$ and only consider the nonnegative solutions $u \geq 0$. Define $t_n = (n - 1)\Delta t$ to be the integration time $0 \leq t_n \leq T$ and $\Delta t = \frac{T}{n_T}$. Let u_{ij}^n be the numerical solution to $u(\hat{\mathbf{x}}_{ij}, t_n)$ and denote $\mathbf{u}^n = \text{vec}(\{u_{ij}^n\}_{ij})$. We denote $(u^m)_{ij}^n = u(\hat{\mathbf{x}}_{ij}, t_n)^m$. Consider the Crank-Nicolson discretization for Eq. (38)

$$\frac{u_{ij}^{n+1} - u_{ij}^n}{\Delta t} + \frac{1}{2}(-\Delta)^s(u^m)_{ij}^{n+1} + \frac{1}{2}(-\Delta)^s(u^m)_{ij}^n = 0$$

To linearize the equation, we consider the same technique used in [25]

$$(u^m)_{ij}^{n+1} \approx (u^m)_{ij}^n + m(u^{m-1})_{ij}^n(u_{ij}^n - u_{ij}^{n-1})$$

Using the matrices in Section 3.3, we have the discretized equation (assuming $\mathbf{u}^{-1} = \mathbf{0}$)

$$\mathbf{u}^{n+1} = \mathbf{u}^n - \frac{m\Delta t}{2}\mathbf{F}^*\mathbf{M}^{*-1}((\mathbf{u}^{m-1})^n \otimes (\mathbf{u}^n - \mathbf{u}^{n-1})) - \frac{\Delta t}{2}\mathbf{F}^*\mathbf{M}^{*-1}(\mathbf{u}^m)^n \quad n = 1, 2, \dots, n_T \quad (39)$$

$$\mathbf{u}^1 = \mathbf{f} \quad (40)$$

where $\mathbf{f} = \text{vec}(\{f(\hat{\mathbf{x}}_{ij})\}_{i,j \in \mathcal{I}_L})$, and \otimes denotes the element-wise multiplication, and

$$\mathbf{M}^* = \mathbf{M}[\mathcal{I}_L, \mathcal{I}_L] \quad \mathbf{L}^* = \mathbf{L}[\mathcal{I}_L, \mathcal{I}_L] \quad (41)$$

In the numerical example, we let $f(\mathbf{x}) = \exp(-100|\mathbf{x}|^2)$, $a = 0.1$, $R = 20$, $h = 1000$, $n_T = 1000$, $\Delta t = 0.0001$, 1000 quadrature points in the radial direction and 20 in the axial direction. Figure 6 shows the changes in the value $u_h(\mathbf{0}, t)$ for $0 \leq t \leq 0.1$ and different m , s . Typically we do not have analytical solutions for general m and s ; however, in the special case when $m = 1$ and $s = 0.5$, we obtain the equation

$$\frac{\partial u}{\partial t} + (-\Delta)^{1/2}u = 0 \quad (42)$$

the linear fractional heat equation has analytical solution through convolution with the explicit Poisson kernel in \mathbb{R}_+^3 (\mathbb{R}^2 spatial and \mathbb{R}_+ temporal) [3]

$$u(\mathbf{x}, t) = c_{1/2,2} \int_{\mathbb{R}^2} \frac{tf(\mathbf{y})}{(|\mathbf{x} - \mathbf{y}|^2 + t^2)^{3/2}} d\mathbf{y} \quad (43)$$

Particularly, we have in our case

$$u(\mathbf{0}, t) = 1 - 10\sqrt{\pi t^2} e^{100t^2} \text{erfc}(10t) \quad (44)$$

The equation Eq. (44) can be used for verification and the values are plotted alongside the numerical results in Figure 6. We can see that the numerical result and the exact solution coincide for $t \in [0, 0.1]$ and $s = 0.2$, $m = 1$. We can also see that the larger the s or the smaller the m , the faster the diffusion is. Different values of s and m provide different profiles of the diffusion process and therefore form a powerful tool for modeling anomalous diffusion. Figure 7 shows the diffusion profile at $t = 0.1$ for different cases.

5. Conclusion

We have numerically studied the application of NURBS-based iso-geometric analysis for PDEs involving the fractional Laplacian operator, and applied the proposed algorithm to solve the fractional porous media equation. This opens a new venue for nonlocal modeling with iso-geometric analysis. Consequently, it is possible to import many favorable features of the iso-geometric analysis such as its ease and precision in defining boundaries (in this work, we worked with both the disk domain and the square domain) [26], higher accuracy per degree of freedom compared with classical Lagrange polynomials for finite element analysis [27], being computationally less costly, seamless integration with CAD tools and no need for several re-meshing during optimization compared with FEM [10].

The proposed algorithm showed promising and satisfactory results on the benchmark problems where monotonous convergence was obtained and a consistent convergence rate was captured throughout multiple test cases. In the porous media equation case the numerical solution coincided with the exact solution when the latter was available. The algorithm delivered results that were consistent with our understanding of anomalous diffusion.

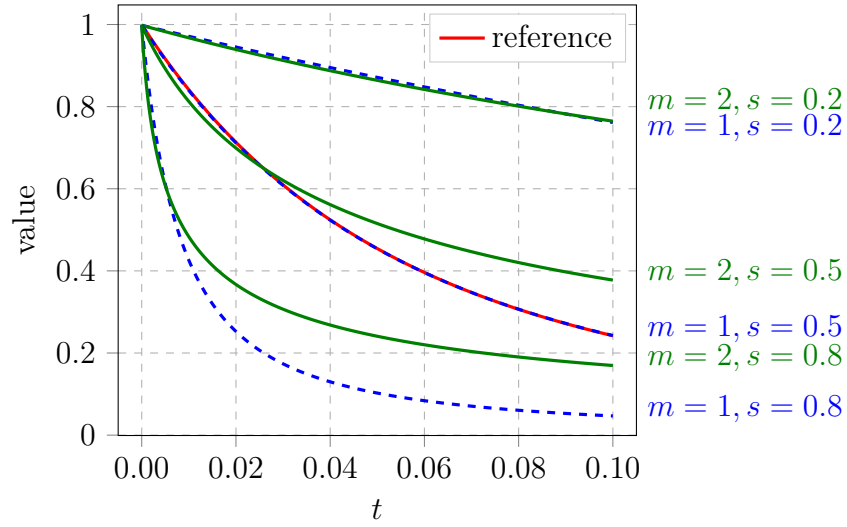


Figure 6: Evolution of $u_h(\mathbf{0}, t)$ in different settings. The numerical results coincide with the exact solution for $m = 1, s = 0.5$. The reference solution is given only for $m = 1, s = 0.5$, because analytical solutions are not available for the other parameters.

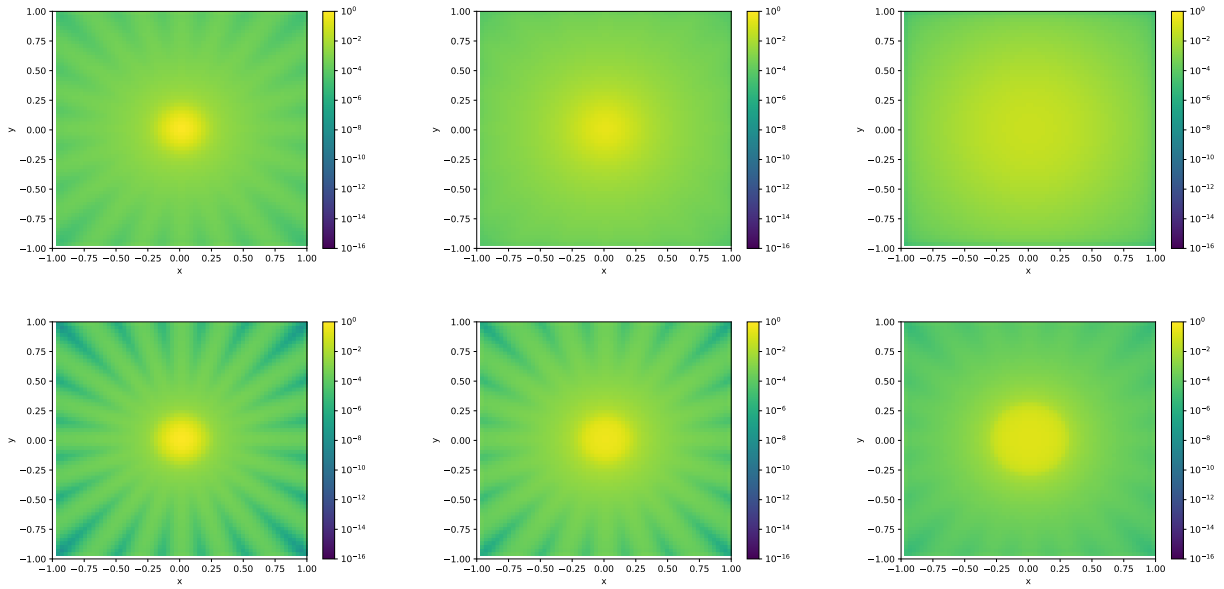


Figure 7: Solution to the porous media equation at $t = 0.1$. First row: $m = 1$, second row: $m = 2$; first column: $s = 0.2$, second column: $s = 0.5$, third column: $s = 0.8$. Note the logarithmic scale for colors.

We conclude that iso-geometric analysis is a viable tool for nonlocal problems in differential equation such as the fractional PDEs. The iso-geometric collocation method is much easier to implement compared to the finite element methods in the case of the fractional Laplacian. In addition, it shows superior accuracy in terms of accuracy per degree of freedom. An important next step is to develop efficient algorithms and explore the potential of iso-geometric analysis for fractional PDEs. For example, the computation of integrals can be accelerated using fast multiple method [28–36].

The appendix includes the basic concepts of iso-geometric analysis which are relevant for our implementation.

Appendix A. Preliminary: Iso-geometric Analysis

Appendix A.1. B-spline

We can describe B-splines in terms of a *knot vector* in the *parameter space*. A knot vector is specified by a non-decreasing set of coordinates

$$\mathcal{U} = \{u_1, u_2, \dots, u_{l+1}\} \quad (\text{A.1})$$

where u_i is called the *knot*, and satisfies

$$0 = u_1 = u_1 = \dots = u_{p+1} \leq u_{p+2} \leq \dots \leq u_{l-p} \leq u_{l-p+1} = u_{l-p+2} = \dots = u_{l+1} = 1 \quad (\text{A.2})$$

We allow the same value to occur multiple times and it will affect the continuity of the B-spline.

The i -th B-spline basis function of p -degree $N_{i,p}$ can be defined recursively as

$$B_{i,0}(u) = \begin{cases} 1 & \text{if } u_i \leq u < u_{i+1}, \\ 0 & \text{otherwise;} \end{cases} \quad (\text{A.3})$$

$$B_{i,p}(u) = \frac{u - u_i}{u_{i+p} - u_i} B_{i,p-1}(u) + \frac{u_{i+p+1} - u}{u_{i+p+1} - u_{i+1}} B_{i+1,p-1}(u) \quad (\text{A.4})$$

We note that B-splines have the following properties:

- The basis $B_{i,p}$ has compact support in $[u_i, u_{i+p+1}]$.
- For a knot vector of size $l + 1$, there are $l - p$ B-spline basis functions in total.
- They form a partition of unity, i.e.,

$$\sum_{i=1}^{l-p} B_{i,p} = 1 \quad (\text{A.5})$$

- Assume that all the inequalities in Eq. (A.2) are strict, then $B_{i,p} \in \mathcal{C}^{p-1}$ but $B_{i,p} \notin \mathcal{C}^p$.

Appendix A.2. NURBS

The NURBS basis function is created from B-splines by

$$N_{i,p}(u) = \frac{w_i B_{i,p}(u)}{\sum_{j=1}^{l-p} w_j B_{j,p}(u)} \quad (\text{A.6})$$

where w_i are $l - p$ weights assigned to each B-spline basis function. Bivariate NURBS are constituted by (suppressing the degrees p and q for u and v)

$$N_{k,l}(u, v) = \frac{w_{kl}B_k(u)B_l(v)}{\sum_{i=1}^{l_u-p} \sum_{j=1}^{l_v-q} w_{ij}B_i(u)B_j(v)} \quad (\text{A.7})$$

where $l_u + 1$ and $l_v + 1$ are the number of knots for u and v knot vectors.

A domain in one-dimension and two-dimension Cartesian space can be constructed with

$$\begin{aligned} X &= F(u) = \sum_{i=1}^{l-p} N_{i,p}(u) \tilde{X}_i \\ \mathbf{X} &= \mathbf{F}(u, v) = \sum_{i=1}^{l_u-p} \sum_{j=1}^{l_v-q} N_{k,l}(u, v) \tilde{\mathbf{X}}_{ij} \end{aligned} \quad (\text{A.8})$$

where \tilde{X}_i and $\tilde{\mathbf{X}}_{ij}$ are called *control points*. The equation Eq. (A.8) defines a mapping from parameter space to the physical space. Figure A.8 shows two examples of 2D domains constructed from NURBS basis functions. The red dots are the control points while the blue patches are subdomains corresponding to $[u_i, u_{i+1}] \times [v_j, v_{j+1}]$ in the parameter space.

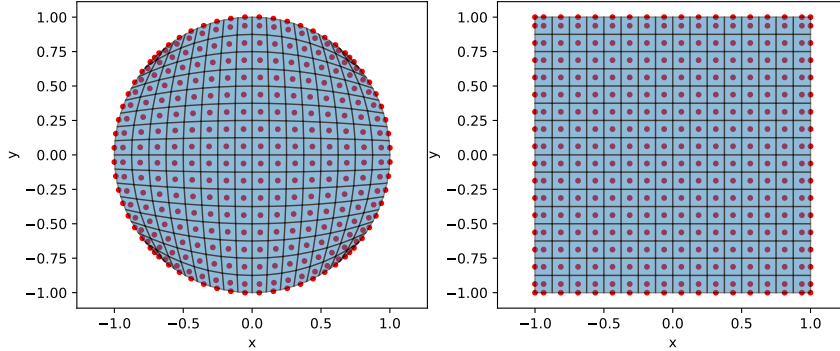


Figure A.8: Two examples of 2D domains constructed from NURBS basis functions. The red dots are the control points while the blue patches are subdomains corresponding to $[u_i, u_{i+1}] \times [v_j, v_{j+1}]$ in the parameter space.

In iso-geometric analysis we use the same functions N_{kl} as basis functions for approximating the solutions. The interpolation function space is defined by a “push forward” operator

$$\mathbf{V} = \text{span}\{N_{kl} \circ \mathbf{F}^{-1}\}_{k=1,2,\dots,l_u-p; l=1,2,\dots,l_v-q} \quad (\text{A.9})$$

i.e., the numerical solution is given by

$$u_h(x, y) = \sum_{i=1}^{l_u-p} \sum_{j=1}^{l_v-q} N_{ij}(\mathbf{F}^{-1}(x, y)) c_{ij} \quad (\text{A.10})$$

where c_{ij} are coefficients determined by solving the governing equations.

Appendix A.3. Knot Insertion

The process of mesh refinement is critical to validate the numerical model. In isogeometric analysis, *knot insertion* provides us a way to easily refine the NURBS mesh. For any NURBS curve in the first formula of Eq. (A.8), we can view it as the projection of a B-spline curve in the two-dimensional space, where the coordinates are given as

$$\bar{\mathbf{X}}_i = [w_i \tilde{X}_i, w_i] \quad (\text{A.11})$$

Given the $l - p$ basis functions and the knot vector $\{u_1, u_2, \dots, u_{l+1}\}$, and $\bar{u} \in [u_k, u_{k+1})$ be a desired new knot, the new $l + 2$ control points $\{\bar{\mathbf{X}}_1^\dagger, \bar{\mathbf{X}}_2^\dagger, \dots, \bar{\mathbf{X}}_{l+2}^\dagger\}$ are formed from the original control points by

$$\bar{\mathbf{X}}_i^\dagger = \alpha_i \bar{\mathbf{X}}_i + (1 - \alpha_i) \bar{\mathbf{X}}_{i-1} \quad (\text{A.12})$$

where

$$\alpha_i = \begin{cases} 1 & 1 \leq i \leq k - p, \\ \frac{\bar{u} - u_i}{u_{i+p} - u_i} & k - p + 1 \leq i \leq k \\ 0 & k + 1 \leq i \leq l + 2 \end{cases} \quad (\text{A.13})$$

The new projected coordinates of the control points in the physical space are obtained using

$$\bar{X}_i^\dagger = \frac{(\bar{\mathbf{X}}_i^\dagger)_1}{(\bar{\mathbf{X}}_i^\dagger)_2} \quad (\text{A.14})$$

where $(\dots)_j$ denotes the j -th component. Knot insertion for two or higher dimension NURBS domains can be done separately for each dimension.

Appendix A.4. Computing the Coordinates in the Parameter Space

In the course of computing the fractional Laplacian, we need to compute the coordinate in the parametric space given its physical space location. NURBS does not provide a direct way to do this and thus a nonlinear equation is usually required to be solved. Specifically, given $\mathbf{x} = \begin{bmatrix} x \\ y \end{bmatrix}$, we want to find (u, v) such that

$$\mathbf{F}(u, v) = \sum_{i=1}^{l_u - p} \sum_{j=1}^{l_v - q} N_{i,j}(u, v) \tilde{\mathbf{X}}_{ij} = \begin{bmatrix} x \\ y \end{bmatrix} \quad (\text{A.15})$$

We can adopt the Gauss-Newton method for solving Eq. (A.15), where the gradient

$$\nabla \mathbf{F}(u, v) = \begin{bmatrix} \frac{\partial F_1}{\partial u} & \frac{\partial F_1}{\partial v} \\ \frac{\partial F_2}{\partial u} & \frac{\partial F_2}{\partial v} \end{bmatrix} \quad (\text{A.16})$$

is required. The gradient can be computed by noticing that

$$\begin{aligned}
S(u, v) &= \left(\sum_{i,j} w_{ij} B_i(u) B_j(v) \right)^2 \\
\frac{\partial N_{kl}(u, v)}{\partial u} &= \frac{w_{kl} B'_k(u) B_l(u) \sum_{i,j} w_{ij} B_i(u) B_j(v) - w_{kl} B_k(u) B_l(v) \sum_{i,j} w_{ij} B'_i(u) B_j(v)}{S(u, v)} \\
\frac{\partial N_{kl}(u, v)}{\partial v} &= \frac{w_{kl} B_k(u) B'_l(v) \sum_{i,j} w_{ij} B_i(u) B_j(v) - w_{kl} B_k(u) B_l(v) \sum_{i,j} w_{ij} B_i(u) B'_j(v)}{S(u, v)}
\end{aligned} \tag{A.17}$$

The algorithm for computing the coordinates in the parameter space is shown in Algorithm 2.

Algorithm 2 Gauss-Newton Method for Computing the Coordinates in the Parameter Space.

```

1: Input:  $\mathbf{x}_0$    Output:  $\mathbf{u}$ 
2: Initialize  $\mathbf{u} \leftarrow \begin{bmatrix} 0.5 \\ 0.5 \end{bmatrix}$ ,  $\mathbf{x} \leftarrow \mathbf{F}(\mathbf{u})$ 
3: while  $|\mathbf{x}_0 - \mathbf{x}| > \text{tolerance}$  do
4:    $\mathbf{d} \leftarrow (\nabla \mathbf{F}(\mathbf{u}))^{-1} (\mathbf{x} - \mathbf{x}_0)$ 
5:    $\mathbf{u} \leftarrow \mathbf{u} - \mathbf{d}$ 
6:    $\mathbf{x} \leftarrow \mathbf{F}(\mathbf{u})$ 
7: end while
8: return  $\mathbf{u}$ 

```

References

- [1] Mateusz Kwaśnicki. Ten equivalent definitions of the fractional laplace operator. *Fractional Calculus and Applied Analysis*, 20(1):7–51, 2017.
- [2] Yufeng Wang, Hui Zhou, Hanming Chen, and Yangkang Chen. Adaptive stabilization for q-compensated reverse time migration. *Geophysics*, 83(1):S15–S32, 2017.
- [3] Arturo de Pablo, Fernando Quirós, Ana Rodríguez, and Juan Luis Vázquez. A fractional porous medium equation. *arXiv preprint arXiv:1001.2383*, 2010.
- [4] Paolo Gatto and Jan S Hesthaven. Numerical approximation of the fractional laplacian via *hp*-finite elements, with an application to image denoising. *Journal of Scientific Computing*, 65(1):249–270, 2015.
- [5] Anna Lischke, Guofei Pang, Mamikon Gulian, Fangying Song, Christian Glusa, Xiaoning Zheng, Zhiping Mao, Wei Cai, Mark M Meerschaert, Mark Ainsworth, et al. What is the fractional Laplacian? *arXiv preprint arXiv:1801.09767*, 2018.
- [6] Gabriel Acosta, Francisco M Bersetche, and Juan Pablo Borthagaray. A short fe implementation for a 2d homogeneous dirichlet problem of a fractional laplacian. *Computers & Mathematics with Applications*, 74(4):784–816, 2017.
- [7] Yiran Xu, Jingye Li, Guofei Pang, Zhikai Wang, and Xiaohong Chen. Radial basis function collocation method for decoupled fractional laplacian wave equations. *arXiv preprint arXiv:1801.01206*, 2018.
- [8] Andreas E Kyprianou, Ana Osojnik, and Tony Shardlow. Unbiased ‘walk-on-spheres’ monte carlo methods for the fractional laplacian. *IMA Journal of Numerical Analysis*, 38(3):1550–1578, 2017.
- [9] Kailai Xu and Eric Darve. Spectral method for the fractional laplacian in 2d and 3d. *arXiv preprint arXiv:1812.08325*, 2018.
- [10] Thomas JR Hughes, John A Cottrell, and Yuri Bazilevs. Isogeometric analysis: CAD, finite elements, NURBS, exact geometry and mesh refinement. *Computer methods in applied mechanics and engineering*, 194(39-41):4135–4195, 2005.
- [11] RL Taylor. Isogeometric analysis of nearly incompressible solids. *International Journal for Numerical Methods in Engineering*, 87(1-5):273–288, 2011.
- [12] F Auricchio, L Beirao Da Veiga, TJR Hughes, A_ Reali, and G Sangalli. Isogeometric collocation methods. *Mathematical Models and Methods in Applied Sciences*, 20(11):2075–2107, 2010.
- [13] Mark Ainsworth and Christian Glusa. Aspects of an adaptive finite element method for the fractional laplacian: a priori and a posteriori error estimates, efficient implementation and multigrid solver. *Computer Methods in Applied Mechanics and Engineering*, 327:4–35, 2017.
- [14] Yanghong Huang and Adam Oberman. Numerical methods for the fractional laplacian: A finite difference-quadrature approach. *SIAM Journal on Numerical Analysis*, 52(6):3056–3084, 2014.
- [15] V. Minden and L. Ying. A simple solver for the fractional Laplacian in multiple dimensions. *ArXiv e-prints*, February 2018.
- [16] I Temizer, P Wriggers, and TJR Hughes. Contact treatment in isogeometric analysis with nurbs. *Computer Methods in Applied Mechanics and Engineering*, 200(9-12):1100–1112, 2011.
- [17] Richard W Johnson. Higher order b-spline collocation at the greville abscissae. *Applied Numerical Mathematics*, 52(1):63–75, 2005.
- [18] Frédéric Gibou and Ronald Fedkiw. A fourth order accurate discretization for the laplace and heat equations on arbitrary domains, with applications to the stefan problem. *Journal of Computational Physics*, 202(2):577–601, 2005.
- [19] Yuri Bazilevs, L Beirao da Veiga, J Austin Cottrell, Thomas JR Hughes, and Giancarlo Sangalli. Isogeometric analysis: approximation, stability and error estimates for h-refined meshes. *Mathematical Models and Methods in Applied Sciences*, 16(07):1031–1090, 2006.
- [20] Xavier Ros-Oton and Joaquim Serra. The dirichlet problem for the fractional laplacian: regularity up to the boundary. *Journal de Mathématiques Pures et Appliquées*, 101(3):275–302, 2014.
- [21] slides.pdf. https://www.uni-muenster.de/AMM/num/Vorlesungen/PDEI_SS14/material/slides.pdf. (Accessed on 05/25/2019).
- [22] Mark Ainsworth and Christian Glusa. Towards an efficient finite element method for the integral fractional Laplacian on polygonal domains. *arXiv preprint arXiv:1708.01923*, 2017.

- [23] Alessandro Reali and Thomas JR Hughes. An introduction to isogeometric collocation methods. In *Isogeometric Methods for Numerical Simulation*, pages 173–204. Springer, 2015.
- [24] Bartłomiej Dyda, Alexey Kuznetsov, and Mateusz Kwaśnicki. Eigenvalues of the fractional laplace operator in the unit ball. *Journal of the London Mathematical Society*, 95(2):500–518, 2017.
- [25] Łukasz Płociniczak. Approximation of the erdélyi–kober operator with application to the time-fractional porous medium equation. *SIAM Journal on Applied Mathematics*, 74(4):1219–1237, 2014.
- [26] Behrooz Hassani, S Mehdi Tavakkoli, and NZ Moghadam. Application of isogeometric analysis in structural shape optimization. *Scientia Iranica*, 18(4):846–852, 2011.
- [27] David Großmann, Bert Jüttler, Helena Schlusnus, Johannes Barner, and Anh-Vu Vuong. Isogeometric simulation of turbine blades for aircraft engines. *Computer Aided Geometric Design*, 29(7):519–531, 2012.
- [28] J Carrier, Leslie Greengard, and Vladimir Rokhlin. A fast adaptive multipole algorithm for particle simulations. *SIAM journal on scientific and statistical computing*, 9(4):669–686, 1988.
- [29] Hongwei Cheng, Leslie Greengard, and Vladimir Rokhlin. A fast adaptive multipole algorithm in three dimensions. *Journal of computational physics*, 155(2):468–498, 1999.
- [30] Naoshi Nishimura, Ken-ichi Yoshida, and Shoichi Kobayashi. A fast multipole boundary integral equation method for crack problems in 3d. *Engineering Analysis with Boundary Elements*, 23(1):97–105, 1999.
- [31] Naoshi Nishimura. Fast multipole accelerated boundary integral equation methods. *Applied mechanics reviews*, 55(4):299–324, 2002.
- [32] JM Song and Weng Cho Chew. Multilevel fast-multipole algorithm for solving combined field integral equations of electromagnetic scattering. *Microwave and Optical Technology Letters*, 10(1):14–19, 1995.
- [33] Eric Darve. The fast multipole method: numerical implementation. *Journal of Computational Physics*, 160(1):195–240, 2000.
- [34] Pieter Coulier, Hadi Pouransari, and Eric Darve. The inverse fast multipole method: using a fast approximate direct solver as a preconditioner for dense linear systems. *SIAM Journal on Scientific Computing*, 39(3):A761–A796, 2017.
- [35] Eric Darve, Cris Cecka, and Toru Takahashi. The fast multipole method on parallel clusters, multicore processors, and graphics processing units. *Comptes Rendus Mecanique*, 339(2-3):185–193, 2011.
- [36] William Fong and Eric Darve. The black-box fast multipole method. *Journal of Computational Physics*, 228(23):8712–8725, 2009.